Available online at www.sciencedirect.com

ScienceDirect

Acta Materialia 77 (2014) 183–190

Acta MATERIALIA

www.elsevier.com/locate/actamat

Characterization of late-stage equiaxed solidification of alloys

David Montiel [a,*], Sebastian Gurevich [a,b], Nana Ofori-Opoku [a,c], Nikolas Provatas [a]

[a] Department of Physics, McGill University, Montreal, QC H3A-2T8 Canada
[b] Department of Chemical Engineering, McGill University, Montreal, QC H3A 0C5, Canada
[c] Department of Mining and Materials Engineering, McGill University, Montreal, QC H3A-0E8, Canada

Received 11 March 2014; received in revised form 28 May 2014; accepted 30 May 2014

Abstract

We use a two-dimensional phase-field model coupled to a nucleation mechanism to study the evolution of interdendritic liquid pools during late-stage solidification of Mg–Al alloys under spatially uniform temperature and constant cooling rates. We obtain the channel size distribution (CSD) of liquid pools at solid fractions close to those where eutectic phase is expected to form and investigate the influence of cooling rate on the morphology of the CSD at different solidification stages. Our results show that the CSD is unimodal, exhibiting a peak at small channel widths followed by a shoulder and longer decay tail at large channel widths. This feature is correlated to the presence of two distinct liquid regions, small channels between secondary branches of the primary phase and larger channels between adjacent grains. We construct a cooling-rate/solid-fraction morphology diagram that shows the relative importance of the shoulder in the CSD. We characterize the mean and standard deviation of the CSD and show that, within the range of data examined, the mean channel size vs. cooling rate curves scale with solid fraction. The numerical tools developed for this work can also be used to analyze experimental results. We include the analysis of two experimental micrographs previously published by Paliwal et al.

Keywords: Phase-field model; Solidification microstructure; Binary alloys; Dendritic growth

1. Introduction

The as-cast microstructure as well as the spatial distribution of solutes that develops during the primary phase of solidification serves as a template for the formation of secondary phases in metal alloys. There has been extensive research on microstructure selection of primary phases during solidification in alloys [1–9] using dynamical experiments and phase-field simulations. The selection of secondary phases is typically predicted by applying thermodynamic models of equilibrium phases to the thermosolutal conditions during late-stage solidification [10,11]. However, to date most such studies usually ignore the role of complex interface topology and liquid pool confinement on the second-phase selection process.

Numerical modeling has become rapid and sophisticated enough to simulate the evolution of very complex interface topologies during solidification, topologies that would otherwise be difficult to observe experimentally, and which can help clarify the mechanisms by which the final properties of alloy phases emerge. For example, using multicomponent and multiphase field models [12–14], it is possible to characterize and measure the distributions of multiple solutes and correlate them to the morphology of liquid channels that form between primary phases throughout the solidification path. By studying interdendritic liquid pools at the stage at which they become precursors of

---

* Corresponding author. Present address: Department of Materials Science and Engineering, University of Michigan, 2300 Hayward St., Ann Arbor, MI 48109, USA. Tel.: +1 734 478 0551.

E-mail addresses: dmontiel@umich.edu (D. Montiel), sebastian.gurevich@mcgill.ca (S. Gurevich), nana.ofori-opoku@mail.mcgill.ca (N. Ofori-Opoku), provatas@physics.mcgill.ca (N. Provatas).

http://dx.doi.org/10.1016/j.actamat.2014.05.063
1359-6454/

secondary phases, it is thus possible to gain insights into the final distribution and type of second phases of the resulting alloy.

In this work we model the liquid pool evolution in the late stages of solidification of a binary alloy of composition Mg–10 wt.%Al under conditions of uniform temperature and constant cooling rate. The aforementioned composition is chosen due to its similarity to AZ91 Mg alloy, which is a well-known commercial alloy the properties of which have been extensively studied [16–19]. Fig. 1 shows two experimental micrographs of Mg–9 wt.%Al for different cooling rates: 30 and 75 K s^{-1} [15]. In both cases the microstructure consists of a convoluted network of narrow second-phase channels between grains of primary phase, a morphology that is typical of dendritic growth. In order to characterize such microstructure, we calculate the channel size distribution (CSD) of the interdendritic liquid channels at solid fractions close to those at which they would become precursors of eutectic phase. The mean channel width, its standard deviation and the structure of the CSD distribution are examined as a function of primary solid fraction and cooling rate. Making the reasonable assumption that the transformation of supersaturated liquid pools into eutectic occurs at much shorter timescales than those that characterize primary phase evolution,[1] we may regard the results of this study as defining a statistical metric for characterizing the distribution of secondary phases. A future publication will address the question of how secondary phases emerge from the liquid during late-stage solidification.

The structure of this paper is as follows. Section 2 introduces the methods we use to simulate the microstructure and solute concentration dynamics, as well as to obtain the CSD. In Section 3 we present and discuss our results regarding the characterization and scaling of interdendritic liquid pools. Finally, in Section 4 we present our conclusions and an outlook on future work.

2. Methods

2.1. Nucleation algorithm

We coupled our phase-field model solidification process to a quantitatively accurate model for nucleation in order to obtain a realistic spatial distribution of grains as well as the undercooling at which they appear. Our model considers heterogeneous nucleation on inoculant particles as the sole mechanism of grain inception. We follow the stochastic coarse graining approach of Simmons et al. [20], already applied successfully in Ref. [21] to a binary alloy. This approach consists of calculating the probability of spontaneous nuclei formation within a certain volume element during a certain time interval. The following expression yields the probability p_N that at least one solid nucleus of critical size forms within a homogeneous volume element ΔV during a time interval Δt:

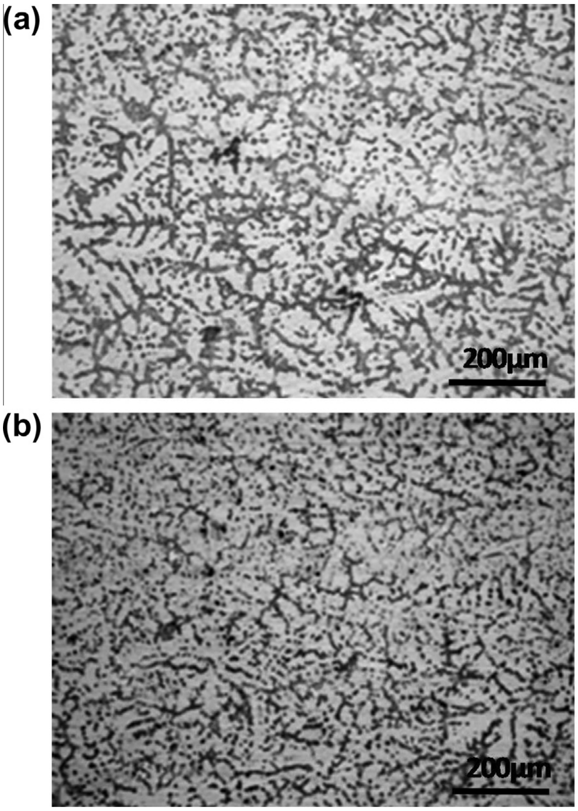

Fig. 1. Optical micrographs of Mg–9 wt.%Al under cooling rates (a) 30 K s^{-1} and (b) 75 K s^{-1}. Reprinted from [15] with permission.

$$p_N = 1 - \exp(-J\Delta V \Delta t), \tag{1}$$

where J is the nucleation rate which depends on the local conditions of the metastable liquid, the physical properties of the material, and the nature and concentration of inoculant particles. The coupling of nucleation to phase-field dynamics that simulate dendritic growth is described in more detail in Ref. [21].

2.2. Phase-field model

We use a phase-field model to simulate growth after nucleation of equiaxed grains of Mg–10 wt.%Al. This model is a modified version of the quantitative phase-field model for dilute binary alloys described in detail in Ref. [22], and further extended for general two-phase polycrystalline binary alloys [23] by Ofori-Opoku et al. [24]. Our model includes thermal noise to promote sidebranching. Details on the inclusion of thermal noise in the model can be found in Refs. [7,25]. We also include non-vanishing, temperature-dependent solute diffusivity in the solid which is responsible for back-diffusion. For the range of temperatures considered, the solute diffusivity varies within two orders of magnitude. The evolution of solidifying domains of primary phase is found by numerical

---

[1] An argument in support of this hypothesis is presented in the discussion of Fig. 4 in Section 3.2.

integration in time of a set of coupled differential equations for solute concentration and order parameter fields. Each order parameter field represents the state (solid or liquid) of a different crystallographic orientation. The model is coupled to the adaptive mesh refinement algorithm [26,27], which allows for a significant improvement in computational efficiency compared to fixed-mesh methods.

2.3. Microstructure analysis

At any given time during the solidification process, the CSD of the liquid domains can be calculated from a global solid–liquid order parameter. For this purpose, we employ a method similar to the one developed in Ref. [28], in which the liquid channels are identified and measured via topological changes of isodistance structures to solid–liquid interfaces. We apply a simpler version of the method for two dimensions with the important difference that we take into account the distribution of all widths within a channel and not only at bottleneck points. This method can be described as follows. First, a global order parameter field $\varphi(\mathbf{r})$ that combines the order parameters of all crystallographic orientations is obtained [24], ranging from -1 (in the liquid) to 1 (in the solid). The values of this field are then interpolated onto a uniform mesh with the smallest grid spacing of the adaptive mesh used for the phase-field simulation. A subsequent interpolation step is performed to obtain a mesh with one further level of refinement. This allows a more precise measurement of small channels on the order of the interface width. The global order parameter is mapped onto a discrete bilevel data set with values $1/2$ in the solid, $-1/2$ in the liquid and discontinuous at the interfaces. Then, using the set level method described in Ref. [28] a signed distance function field $d(\mathbf{r})$ is calculated. The function $d(\mathbf{r})$ has the same sign as the global order parameter (except at the interface, where it is zero) and its magnitude represents the Euclidian distance from each point to the nearest interface. The signed distance function is smoothed with a three-point boxcar-averaging method. It follows, from the definition of $d(\mathbf{r})$, that its value at each point along a line that goes through the middle of a channel is a measure of half the channel width. We can identify the line that runs along the middle of a channel as the set of points for which ∇d is discontinuous. Moreover, the distance function must satisfy the condition $|\nabla d| = 1$ elsewhere. Thus, once the distance function is found, the location of the mid-channel lines can be obtained by calculating ∇d using a simple central difference scheme and identifying the grid points for which $|\nabla d| < \delta$, where δ is a threshold value less than unity. We found that the value $\delta = 0.9$ works well. Fig. 2 shows two examples in which the mid-channel locations have been found and marked. They correspond to simulation domains formed at a cooling rate of 80 K s^{-1}, when the solid fraction reaches 0.85 (a) or 0.55 (b). Note that this method is only applicable when channel-like structures (i.e., thin, elongated liquid pools) are prevalent, which is only the case at high solid fractions. Thus, the CSD calculation loses accuracy for low solid fractions, where large liquid regions are present between grains. Fig. 2b shows an example of a marginally low solid fraction. We set this to be the lowest solid fraction considered in our analysis. Finally, by sampling $d(\mathbf{r})$ along all mid-channel points in the liquid, the CSD is obtained via an appropriate binning scheme.

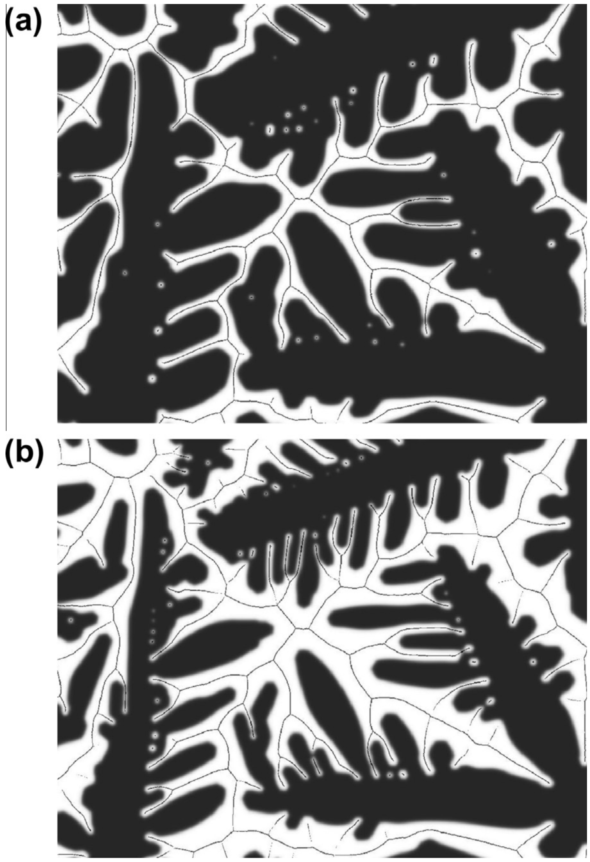

Fig. 2. Mid-channel lines along liquid (white) channels. Obtained from simulation domains formed at a cooling rate of 80 K s^{-1}, and at solid fractions (a) 0.85 and (b) 0.55.

3. Results and discussion

3.1. Parameters examined

We performed 2-D simulations of dendritic growth of solid α phase of an Mg–10 wt.%Al alloy from its undercooled melt under uniform temperature and cooled at a constant rate (Q) from the liquidus temperature. We chose a system size of 520 μm × 520 μm for all simulations. The material, process and model parameters are reported in Table 1. To simulate heterogeneous nucleation we seeded the liquid with a uniformly random inoculant density of 9×10^{-5} μm^{-2} within the initial liquid phase. For simplicity, we assign each grain that nucleates to one of five predetermined orientation values.

Five cooling rates were studied: 10, 50, 80, 100 and 125 K s^{-1}. Beyond this range, interface kinetics begin to dominate the sharp-interface description of the phase-field equations. We sampled the order parameter and solute

Table 1
Physical properties of Mg–10 wt.%Al, phase-field and nucleation parameters used in the simulations.

Physical properties of Mg–10 wt.%Al alloy	
Chemical composition (wt.%)	Al: 10, Mg: 90
Melting point of Mg (°C)	650
Liquidus slope (°C wt.%$^{-1}$)	−6.454
Partition coefficient	0.364
Eutectic temperature (°C)	437
Solute diffusivity (liquid; m^2 s^{-1})	1.8×10^{-9}
Solute diffusivity (solid): $D_s = Ae^{-E_a/(RT)}$	
Prefactor, A (m^2 s^{-1})	3.9×10^{-3}
Activation energy, E_a (J mol^{-1})	1.55×10^5
Gibbs–Thomson coefficient (K m)	6.2×10^{-7}
Density (kg m^{-3})[a]	1740
Solid–liquid interfacial energy (J m^{-2})	0.115
Specific heat (J kg^{-1} K^{-1})[a]	1360
Specific heat of fusion (J kg^{-1})[a]	3.7×10^5
Thermal conductivity (W m^{-1} K^{-1})[a]	78
Thermal diffusivity (m^2 s^{-1})[a]	3.73×10^{-5}
Phase-field simulation parameters	
Effective interface width, W_0 (m)	4×10^{-7}
Minimum grid spacing	$0.781\ W_0$
Anti-trapping coefficient	$1/(2\sqrt{2})$
Nucleation parameters	
Zeldovich factor, Z	0.1
Characteristic frequency, β (s^{-1})	10^{12}

[a] Values for pure Mg.

concentration at intervals of 2 K in temperature drop. For each cooling rate, an ensemble of 20 runs with identical solidification conditions but different random initialization conditions was produced. Thus, all simulations of a given cooling rate and at a given time exhibit the same statistical features but different specific grain positions and orientations. Using the method described in Section 2.3, we calculated the CSD of samples from each ensemble of each cooling rate, at five different solid fractions: 0.55, 0.65, 0.75, 0.85 and 0.9. The CSD for each set of conditions was averaged over the ensemble runs of each cooling rate. The methods developed for this work can also be applied to analyze microstructures obtained in experiments by setting a threshold to the color map range of an image to distinguish between phases. In this way, we obtain the CSDs of the two experimental micrographs shown in Fig. 1, which correspond to an alloy with similar composition to the one we use in our simulations. From these CSDs we extract the mean channel size and standard deviation, and compare the results to those from our simulations.

To estimate the solid fraction at which eutectic phase is expected to appear, we calculated the dependency of solid fraction on undercooling. Fig. 3a shows this dependency for each cooling rate, where each curve is obtained by ensemble-averaging the solid fraction data at each undercooling. As a reference, we also obtained the solid fraction dependence with undercooling under Scheil solidification, which corresponds to the limiting case $Q \rightarrow 0$ and no solute diffusion in the solid. As Fig. 3b shows, the solid fraction ϕ^* corresponding to when the eutectic undercooling ΔT_E is reached does not depend strongly on cooling rate and is close to 0.85 for all values within our range of study.

3.2. Liquid pool concentration

Fig. 4a shows the evolution of the average solute concentration in the liquid ($\overline{C_L}$) as temperature drops from the liquidus point to below T_E for all cooling rates. In all cases, the liquid composition deviates from its equilibrium value only at early stages; whereas at late stages, and well before T_E is reached, $\overline{C_L}$ follows the liquidus line (L). This behavior suggests that once free growth ends and the coarsening stage sets in, the composition in the liquid is uniform and back-diffusion to the solid effectively shuts down due to the temperature dependence of the diffusion coefficient. This is further confirmed by Fig. 4b, showing the evolution with undercooling of the standard deviation around the average of the liquid composition ($\sigma_c = \langle (C_L - \overline{C_L})^2 \rangle^{1/2}$) which is a measure of the spacial inhomogeneity of the solute in the liquid. The spacial uniformity of liquid

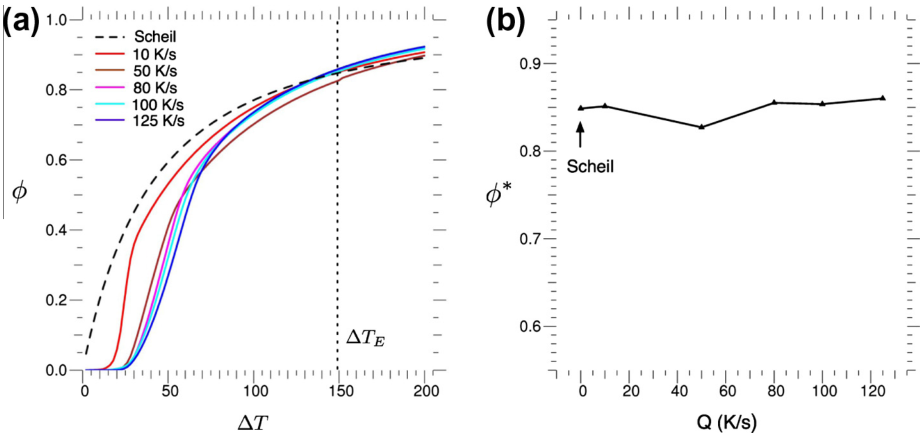

Fig. 3. (a) Ensemble-averaged solid fraction ϕ vs. temperature undercooling ΔT for all cooling rates. The undercooling corresponding to the eutectic temperature is $\Delta T_E = 148.5$ K. (b) Solid fraction ϕ^* for which eutectic undercooling is reached vs. cooling rate. The Scheil (reference) value is $\phi^*_{Scheil} = 0.848$.

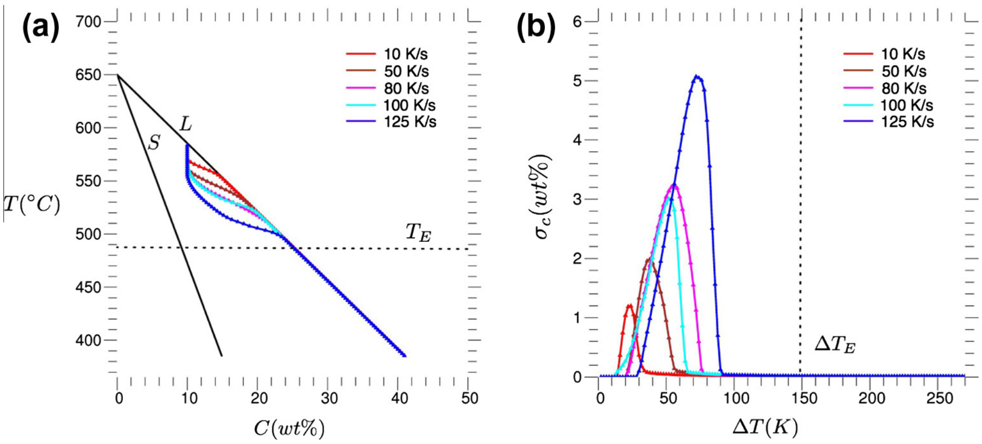

Fig. 4. (a) Evolution of the average solute composition in the liquid ($\bar{C}_L$) with temperature for all cooling rates. The symbols L and S represent, respectively, the liquidus and solidus lines of the dilute limit Mg–Al phase diagram. (b) Standard deviation (σ_c) around the average of the liquid composition vs. temperature undercooling ΔT for all cooling rates.

composition below T_E, along with the assumption of uniform temperature throughout the system implies that the driving force for eutectic formation is also uniform. This, in turn, reinforces the hypothesis that the formation of eutectic phase is almost instantaneous throughout the sample relative to the evolution of primary phase and, therefore, that the late-stage distribution of liquid domains is preserved (or “fossilized”) by secondary phases (e.g. eutectics and intermetallics) that emerge from the liquid at late stages of solidification.

3.3. Evolution of channel size distribution

Fig. 5 shows typical microstructure maps and corresponding CSDs for two cooling rates (10 and 100 K s^{-1}) at two solid fractions (0.65 and 0.85). We define the channel size d_{ch} as half of its width. As expected, the average liquid channel size decreases with solid fraction, while for a given solid fraction, higher cooling rates result in a larger proportion of narrower channels due to enhanced side-branching. The latter effect also lowers the mean channel size of the sample. In Fig. 5, we note that the distributions corresponding to a solid fraction of 0.65 feature a peak at low values of d_{ch} that is relatively sharper than the rest of the distribution. This peak, along with an adjacent shoulder, are features of the distributions present at the lower solid fractions in our analysis. The appearance of the peak is correlated to the length scale of liquid channels between secondary branches that is, on average, smaller than the length scale of liquid channels between different grains. We can therefore interpret the peak and shoulder characteristics as the result of two partial contributions that arise from different features: a broad distribution from the liquid channels between grains, and a sharper distribution (the

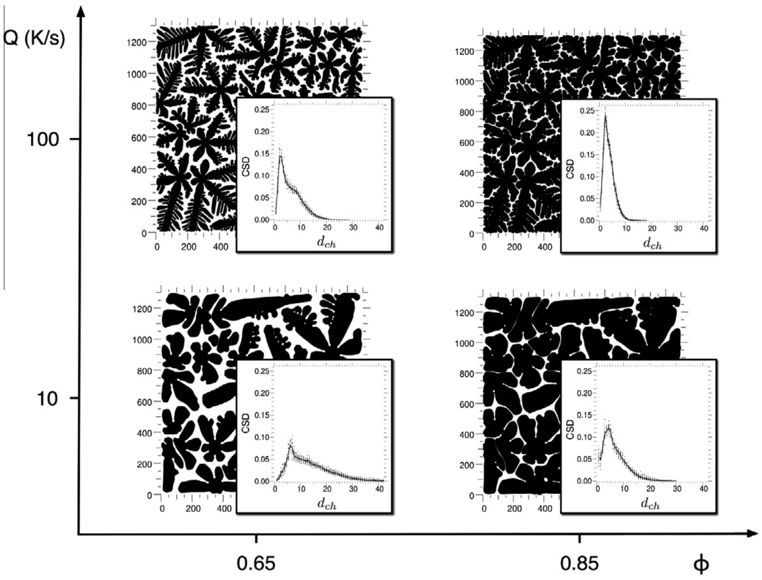

Fig. 5. Phase-field order parameter maps of the solidification microstructure and their corresponding CSDs for cooling rates $Q = 100\ \mathrm{K\ s^{-1}}$ and $Q = 10\ \mathrm{K\ s^{-1}}$ at solid fractions $\phi = 0.65$ and $\phi = 0.85$, respectively. All distances are in units of W_0.

peak) from the narrower channels between secondary branches. When the shoulder is more pronounced, there is a larger difference in breadth between these partial distributions. For the values of Q and ϕ considered, it was found that the shoulder is less prominent at larger solid fractions, which is consistent with the fact that the observed channels between secondary branches and those between grains are comparable in size. Although not as important as solid fraction, cooling rate also has an effect, with higher cooling rates leading to slightly more prominent peaks.

We found that a convenient parameter to quantify the predominance of a peak and shoulder feature in the CSD is the excess kurtosis, defined as $\gamma_2 = \mu_4/\sigma^4 - 3$, where μ_4 is the fourth moment around the mean and σ is the standard deviation. A CSD featuring a prominent peak followed by a shoulder has a smaller kurtosis, while a simple peak without a shoulder yields a higher kurtosis. Fig. 6 shows a morphological state diagram that maps the prominence of the shoulder in the CSD for the values of Q and ϕ examined in this study. As the diagram indicates, the "peak-shoulder" feature appears predominantly in CSDs corresponding to solid fractions below 0.85.

3.4. Channel size scaling

Useful quantitative information about the CSD can be found through its moments. Fig. 7 shows the mean channel size μ and standard deviation σ of each distribution as a function of cooling rate for every solid fraction. The values of μ and σ extracted from the CSD of the two experimental micrographs in Fig. 1 are also shown. The reported solid fraction was calculated as the relative area of the light gray domains with respect to the total area.

As expected from the above discussion, both the mean and standard deviation of the channel size decrease with solid fraction, reflecting that liquid channels become

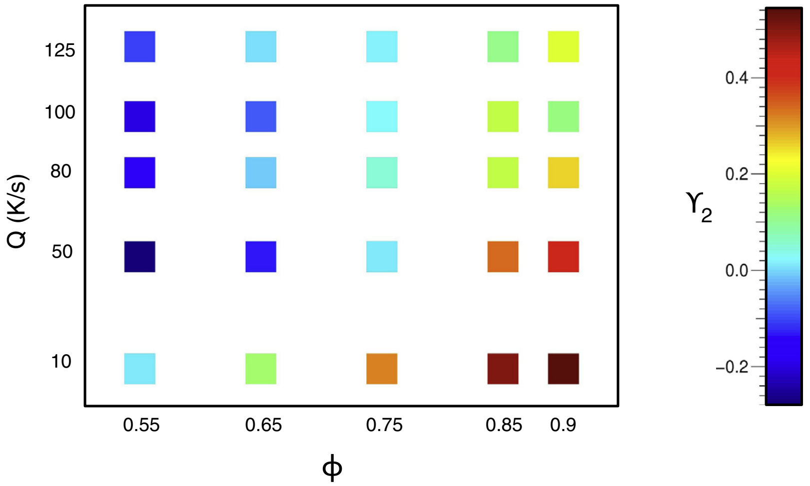

Fig. 6. Cooling rate–solid fraction diagram mapping the kurtosis of the CSD, which measures the prominence of a shoulder in the CSD. Low kurtosis (blue) indicates a prominent peak followed by a shoulder in the CSD, while high kurtosis (red) indicates a simple peak in the CSD. (For interpretation of the references to colour in this figure legend, the reader is referred to the web version of this article.)

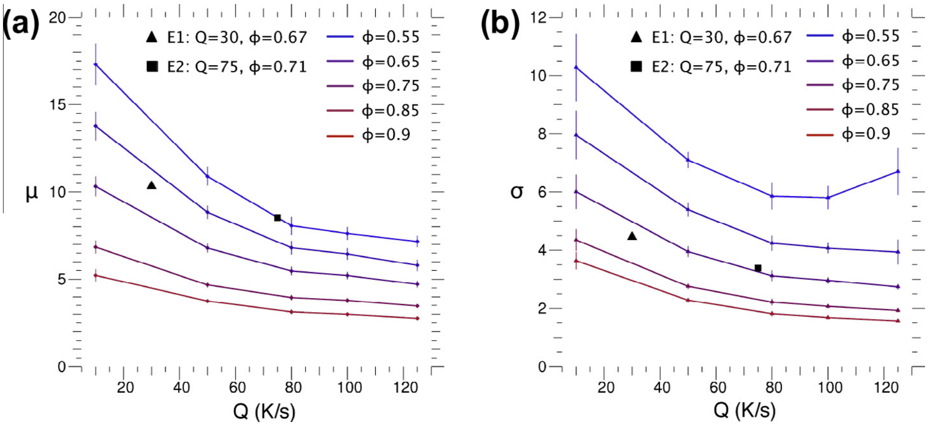

Fig. 7. Mean channel size μ (a) and standard deviation σ (b) as a function of cooling rate for different solid fractions. The length of the error bars equals one standard deviation around the ensemble-averaged values. Points labeled E1 and E2 correspond to the values extracted from the experimental micrographs at cooling rates 30 and 75 K s^{-1}, respectively.

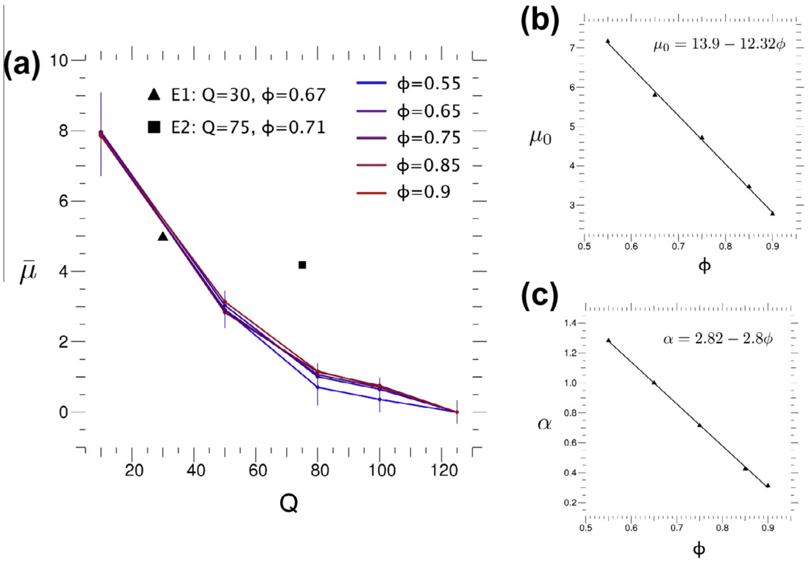

Fig. 8. (a) Mean channel size vs. cooling rate curves collapsed via the transformation given by Eq. (2). Plots of μ_0 (b) and α (c) vs. solid fraction with their respective linear fits (solid lines). Points labeled E1 and E2 correspond, respectively, to the values of $\bar{\mu}$ calculated for the experimental micrographs at cooling rates 30 and 75 K s^{-1}.

narrower and more uniform in width as solidification progresses. The plots also show a decrease in mean channel size with increasing cooling rate. This is consistent with increased sidebranching at higher cooling rates, which increases the tortuosity of the microstructure and, thus, the total length of liquid channels. The standard deviation shows the same qualitative behavior except for the curve at the lowest solid fraction (0.55) which does not decrease monotonically with cooling rate. We believe this could be an artifact of the method we use to compute channel widths which, as discussed in Section 2.3, is less accurate for low solid fractions.

It was found that the mean channel size curves of Fig. 7a can be collapsed into a single master curve $\bar{\mu}$ that depends only on cooling rate via the following scaling relation:

$$\bar{\mu}(Q) = \frac{\mu(Q,\phi) - \mu_0(\phi)}{\alpha(\phi)}, \tag{2}$$

where μ_0 is a vertical offset given by the last value of every curve, i.e. the value of μ corresponding to the highest cooling rate. The parameter α is a scaling factor. Both μ_0 and α depend only on the solid fraction and we found this dependence to be approximately linear in both cases. Fig. 8a shows the curves from Fig. 7a collapsed via the scaling relation in Eq. (2). The same scaling transformation was applied to the values of μ obtained from the experimental samples. Fig. 8b and c show the respective dependence of μ_0 and α on solid fraction for all values of ϕ considered, along with the linear regression fits for each. It is noteworthy that for the fits of both μ_0 and α, the intercept and slope values are close to each other and, in the case of α, almost identical. This implies that the mean channel size scales approximately with liquid fraction, $\phi_L = 1 - \phi$, and that ϕ_L is a more suitable scaling variable than ϕ. Thus, we can rewrite Eq. (2) as:

$$\mu(Q,\phi_L) \simeq f(Q)\phi_L + c, \tag{3}$$

where c is a constant offset and $f(Q)$ is a function of cooling rate only. Substitution of the fitting parameters for μ_0 and α yields $f(Q) = 2.8\bar{\mu}(Q) + 12.32$ and $c = 1.58$. Note that c being close to unity implies that it is of the order of the solid–liquid interface width, W_0, which is the smallest physically meaningful feature that can be resolved in the simulations.

4. Conclusions

This work used phase-field simulations to characterize the evolution of the CSD of interdendritic liquid pools during late-stage solidification. The CSD function was shown to be able to unambiguously distinguish two underlying length scales of liquid pool microstructure: one corresponding to the length scale of channels between secondary branches, and the other to liquid channels between grains. The "signature" of the first length scale manifests itself in a sharp peak at small length scales of the CSD, while the emergence of larger length scales is accompanied by a long-decay tail in the CSD.

From the CSD we were also able to calculate the mean channel size and standard deviation. It was found that the mean channel size dependence with cooling rate scales with the liquid fraction of the system. Specifically, the average channel size dependence on cooling rate and liquid fraction can be decoupled as the product of the liquid fraction and a scaling curve which depends only on cooling rate.

We computed the CSD, the mean channel size and its standard deviation from optical micrographs of experimental castings of a Mg–9 wt.%Al alloy at two cooling rates comparable to those of our simulations. The scaled mean channel size was found to lie approximately on the master curve for the 30 K s^{-1} sample. We believe the discrepancy observed for the high cooling rate (75 K s^{-1}) sample may be, at least in part, due to the limited resolution of the micrograph, which does not allow an accurate measurement of narrow channels. The same argument could explain the discrepancy between the calculated and expected values of the standard deviation. However, a quantitative comparison to experimental results should in principle be possible provided that samples at sufficiently high resolution are available. We also expect a discrepancy due to the 3-D nature of the experimental samples vs. the 2-D nature of our simulations. An upcoming work in 3-D, as well as new experiments, are underway to further investigate this discrepancy.

Since secondary phases appear on relatively short time scales compared to the primary solidification process, the structure of liquid channels at the late stages of solidification essentially forms the template from which eutectic and intermetallic phases will be patterned. In light of these assumptions, the findings of this study suggest the possibility of a universal descriptor of second-phase size distribution that depends only on cooling rate and which scales in a simple way with primary solid fraction at the time of second-phase formation.

The ubiquitous dendritic patterning we see in our simulations of binary alloys is also known to be present in multicomponent alloys. It is thus plausible that the concept of a characteristic CSD is also applicable to more complex alloys. However, the interdiffusion between different components is likely to have a more complex effect on the channel size and distribution. The CSD and its structure for multicomponent alloys will be the subject of an upcoming paper.

Acknowledgments

We thank the Natural Sciences and Engineering Council of Canada and Novelis Global Technology Centre for Funding and the McGill HPC Centre and Compute Canada for Computing Resources.

References

[1] Langer JS. Rev Mod Phys 1980;52:1–28.
[2] Burden MH, Hunt JD. J Cryst Growth 1974;22:99–108.
[3] Burden MH, Hunt JD. J Cryst Growth 1974;22:109–16.
[4] Hunt JD. Cellular and primary dendrite spacings. In: Proceedings of the conference on solidification and casting of metals, Sheffield, July 1977. London: Metals Society; 1979, p. 3–9.
[5] Ben-Jacob E, Garik P. Nature 1990;343:523–30.
[6] Trivedi R, Liu S, Williams S. Nat Mater 2002;1(3):157–9.
[7] Amoorezaei M, Gurevich S, Provatas N. Acta Mater 2010;58:6115–24.
[8] Haxhimali T, Karma A, Gonzales F, Rappaz M. Nat Mater 2006;5:660–4.
[9] Gurevich S, Karma A, Plapp M, Trivedi R. Phys Rev E 2010;81:011603.
[10] Plapp M, Karma A. Phys Rev E 2002;66:061608.
[11] Kim SG, Kim WT, Suzuki T, Ode M. J Cryst Growth 2004;261(1):135–58.
[12] Steinbach I, Pezzolla F. Phys D: Nonlin Phenom 1999;134(4):385–93.
[13] Tiaden J, Nestler B, Diepers H, Steinbach I. Phys D: Nonlin Phenom 1998;115(1–2):73–86.
[14] Suzuki T, Ode M, Kim SG, Kim WT. J Cryst Growth 2002;237–239(Part 1(0)):125–31.
[15] Paliwal M, Kang DH, Essadiqi E, Jung I. Adv Mater Res 2012;409:362–7.
[16] Prakash DG, Regener D. J Alloys Compd 2008;461(1):139–46.
[17] Kabirian F, Mahmudi R. Metall Mater Trans A 2009;40(1):116–27.
[18] Park SS, Park YS, Kim NJ. Met Mater Int 2002;8(6):551–4.
[19] Srinivasan A, Pillai UTS, Pai BC. Metall Mat Trans A 2005;36(8):2235–43.
[20] Simmons J, Shen C, Wang Y. Scripta Mater 2000;43:935–42.
[21] Montiel D, Liu L, Xiao L, Zhou Y, Provatas N. Acta Mater 2012;60(16):5925–32.
[22] Echebarria B, Folch R, Karma A, Plapp M. Phys Rev E 2004;70:061604.
[23] Tong C, Greenwood M, Provatas N. Phys Rev B 2008;77(6):064112.
[24] Ofori-Opoku N, Provatas N. Acta Mater 2010;58:2155–64.
[25] Echebarria B, Karma A, Gurevich S. Phys Rev E 2010;81:021608.
[26] Provatas N, Goldenfeld N, Dantzig J. J Comput Phys 1999;148(1):265–90.
[27] Greenwood M. Using phase-field modeling with adaptive mesh refinement to study elasto-plastic effects in phase transformations, Ph.D. thesis. McMaster University; 2008.
[28] Chan V, Thornton K. Acta Mater 2012;60:2509–17.